Giant Exchange-Bias-Like Effect at Low Cooling Fields Induced by Pinned Magnetic Domains in Y_2NiIrO_6 Double Perovskite

Zheng Deng,* Xiao Wang, Mengqin Wang, Feiran Shen, Jine Zhang, Yuansha Chen, Hai L. Feng, Jiawang Xu, Yi Peng, Wenmin Li, Jianfa Zhao, Xiancheng Wang, Manuel Valvidares, Sonia Francoual, Olaf Leupold, Zhiwei Hu, Liu Hao Tjeng, Man-Rong Li, Mark Croft, Ying Zhang, Enke Liu, Lunhua He, Fengxia Hu, Jirong Sun, Martha Greenblatt,* and Changqing Jin*

Exchange bias (EB) is highly desirable for widespread technologies. Generally, conventional exchange-bias heterojunctions require excessively large cooling fields for sufficient bias fields, which are generated by pinned spins at the interface of ferromagnetic and antiferromagnetic layers. It is crucial for applicability to obtain considerable exchange-bias fields with minimum cooling fields. Here, an exchange-bias-like effect is reported in a double perovskite, Y_2NiIrO_6, which shows long-range ferrimagnetic ordering below 192 K. It displays a giant bias-like field of 1.1 T with a cooling field of only 15 Oe at 5 K. This robust phenomenon appears below 170 K. This fascinating bias-like effect is the secondary effect of the vertical shifts of the magnetic loops, which is attributed to the pinned magnetic domains due to the combination of strong spin–orbit coupling on Ir, and antiferromagnetically coupled Ni- and Ir-sublattices. The pinned moments in Y_2NiIrO_6 are present throughout the full volume, not just at the interface as in conventional bilayer systems.

1. Introduction

The exchange-bias (EB) effect has important applications in spintronic technologies such as spin valves and magnetic tunnel junctions in high-density storages and magnetic switching for logic devices.[1–6] In a conventional EB bilayer, magnetic moments of the ferromagnetic (FM) layer are coupled with interfacial antiferromagnetic (AFM) spins to obtain extra magnetic fields for rotating the whole FM moments.[7] Correspondingly, the magnetic hysteresis loops shift horizontally along the field axis.[8] The pinned uncompensated moments play a dominant role in determining bias magnitude, but only a small fraction of the interfacial

Z. Deng, M. Wang, J. Zhang, Y. Chen, H. L. Feng, J. Xu, Y. Peng, W. Li,
J. Zhao, X. Wang, Y. Zhang, E. Liu, L. He, F. Hu, J. Sun, C. Jin
Institute of Physics
Chinese Academy of Sciences
School of Physics
University of Chinese Academy of Sciences
Beijing 100190, P. R. China
E-mail: dengzheng@iphy.ac.cn; Jin@iphy.ac.cn
Z. Deng, M. Greenblatt
Department of Chemistry and Chemical Biology
Rutgers the State University of New Jersey
E-mail: 123 Bevier Road, Piscataway, NJ 08854, USA;
greenbla@chem.rutgers.edu
X. Wang, Z. Hu, L. H. Tjeng
Max Planck Institute for Chemical Physics of Solids
Nöthnitzer Straße 40, Dresden 01187, Germany
F. Shen
Spallation Neutron Source Science Center
Institute of High Energy Physics
Chinese Academy of Sciences
Dongguan 523803, P. R. China

M. Valvidares
ALBA Synchrotron Light Source
Cerdanyola del Valles
Barcelona 08290, Spain
S. Francoual, O. Leupold
Deutsches Elektronen-Synchrotron (DESY)
Notkestraße 85, Hamburg 22607, Hamburg, Germany
M.-R. Li
Key Laboratory of Bioinorganic and Synthetic Chemistry of
Ministry of Education
School of Chemistry
Sun Yat-Sen University
Guangzhou 510275, P. R. China
M. Croft
Department of Physics and Astronomy
Rutgers the State University of New Jersey
136 Frelinghuysen Road, Piscataway, NJ 08854, USA
L. He
Spallation Neutron Source Science Center
Songshan Lake Materials Laboratory
Dongguan 523808, P. R. China

spins are pinned.[9–10] Such mechanism usually demands large cooling fields (H_{FC}) to obtain sufficient EB fields, adverse to the applications of EB based devices.

Although a large number of studies of EB have been devoted in heterojunctions or core/shell nanoparticles, there are still technical challenges to achieve good performance due to the sensitivity of high quality interfaces.[6,11–12] Alternatively, single-phase bulk materials with magnetic sublattices could be suitable solutions.[13–15] Recently, there has been an interest in single phase materials with vertical magnetic shifts (VMS) of hysteresis loops, which lead to a secondary effect of asymmetry of intercepts on the H-axis, manifesting sizeable EB-like fields. Representative compounds include $Mn_{3.5}Co_{0.5}N$ antiperovskite, Fe_xNbS_2 embedded antiferromagnet and $Ca_{1-x}Sr_xIrO_3$ post-perovskite. $Mn_{3.5}Co_{0.5}N$ has a giant EB-like field of 1.2 T with $H_{FC} = 500$ Oe, while a large EB-like effect was found with cooling field of dozens of Oersteds in $Ca_{1-x}Sr_xIrO_3$.[15–19] The pursuit of smaller H_{FC} for generating large EB fields motivates further research in this field.

Double perovskites, $A_2B''B'''$, provide ideal models to investigate intriguing magnetic properties resulting from multiple magnetic coupling between two different B-site magnetic cations. In this work we show that the ordered orbital moments and strong spin–orbit coupling (SOC) of Ir^{4+} ($5d^5$) lock magnetic moments in a double perovskite, Y_2NiIrO_6 (YNIO). The rock-salt ordered Ni- and Ir-sublattices exhibit long-range ferrimagatic (FiM) ordering below 192 K. The pinned magnetic

moments, which are validated by magnetic force microscopy (MFM) measurements, directly lead to VMS and a giant EB-like effect of 1.1 T induced by a very small cooling field of 15 Oe.

2. Results and Discussion

2.1. Crystal Structure and Valence States

The combination of time-of-flight neutron powder diffraction (NPD), powder X-ray diffraction (PXD) refinements and transmission electron microscopy, indicate that YNIO is a typical B-site rock-salt ordered double perovskite with monoclinic $P2_1/n$ symmetry (**Figure 1**a, and Figures S1 and S2, Supporting Information). The obtained crystallographic parameters are tabulated in Table S1 (Supporting Information) (also see the discussion in Note 1, Supporting Information). Ni and Ir order nearly completely with a small antisite ratio of 7.5%. X-ray absorption spectroscopy (XAS) was used to establish the valence states. In Figure S3a (Supporting Information), the Ni-$L_{2,3}$ peaks locate at the same energies for YNIO and NiO, which is a Ni^{2+} reference material, confirming Ni^{2+} state in YNIO.[20–22] The characteristic multiplet structure at the $L_{2,3}$ edges indicates a Ni^{2+} high-spin state ($3d^8$, $t_{2g}^6 e_g^2$, $S = 1$). Analogously, the same energy of the Ir-L_3 peaks for both YNIO and reference material of $CaCu_3Ir_4O_{12}$ (Figure S3b, Supporting Information) supports
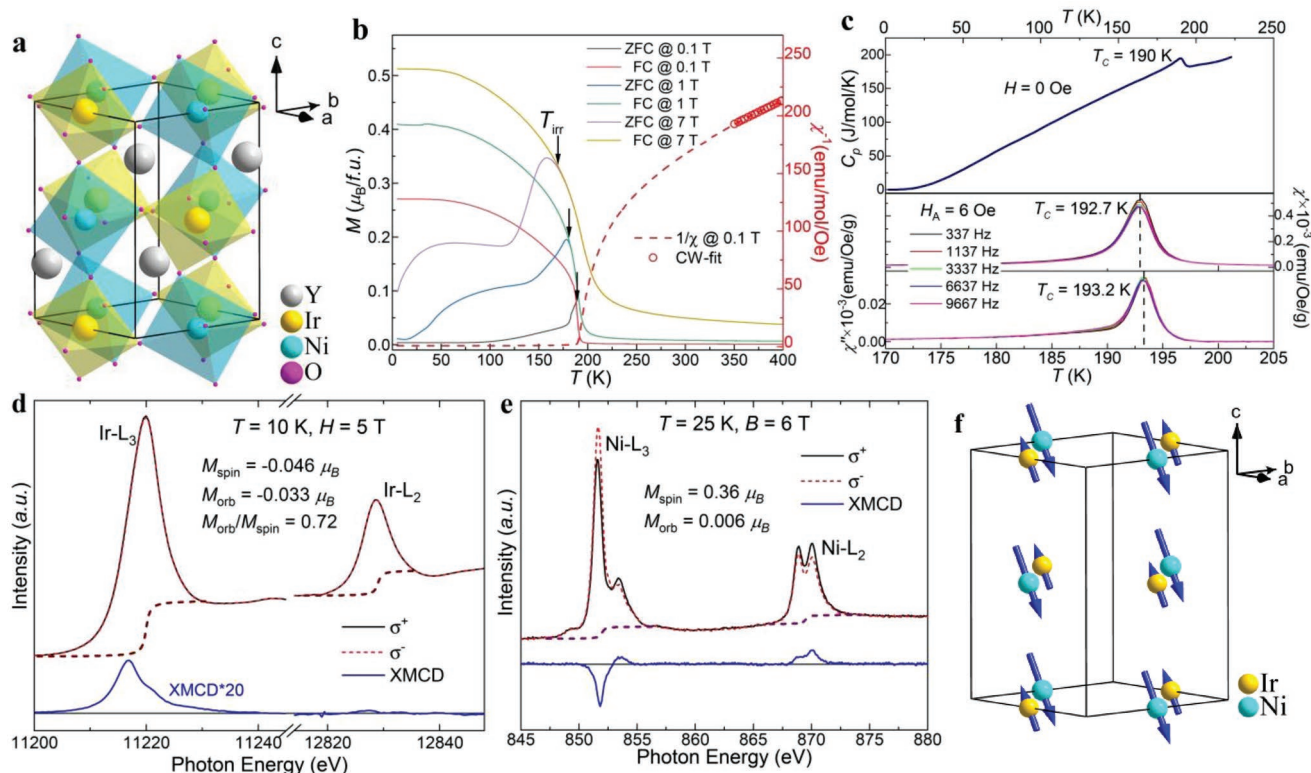

Figure 1. Crystal structure, magnetic properties, and magnetic structure of YNIO. a) Schematic crystal structure of YNIO, showing tilting NiO_6–IrO_6 octahedra. b) $M(T)$ at varying fields (left y-axis) and inverse susceptibility ($\chi^{-1}(T)$) at $H = 0.1$ T (right y-axis). c) Top: $C_p(T)$ at zero field; bottom: $\chi'(T)$ and $\chi''(T)$ with frequency from 337 to 9667 Hz and ac field of 6 Oe. d) Ir-$L_{2,3}$ XMCD at 10 K and 5 T. e) Ni-$L_{2,3}$ XMCD at 25 K and 6 T. f) Schematic magnetic structure of YNIO with antiparallel Ni and Ir moments.

2209759 (2 of 8)

the Ir^{4+} state in YNIO.[23–25] The bond valence sums also indicate the valence states of Ni^{2+} and Ir^{4+}.

2.2. Magnetic Transition and Magnetic Structure

Because of the high cooling-field-sensitivity of YNIO, measurements after zero field cooling (ZFC) in this work were performed after carefully balancing the residual field that is trapped in the superconducting magnet. Figure 1b shows the temperature dependence of magnetization ($M(T)$) after ZFC and field cooling (FC) protocols under fields of 0.1, 1 and 7 T respectively. Upon cooling down, the magnetization rapidly increases to a ferromagnetic-like transition (T_C) at ≈192 K. All the curves exhibit large irreversibility between ZFC and FC processes. Similar magnetic behaviors were usually attributed to glass-like or short range ordering transitions.[26] However, a robust "λ"-shape peak at 190 K is observed on temperature dependence of specific heat ($C_P(T)$) in Figure 1c. In addition, ac susceptibilities ($\chi'(T)$ and $\chi''(T)$) demonstrate frequency-independent peaks at 192 K. These results indicate long-range magnetic ordering rather than a glass-like transition. Thus, we propose that the irreversibility in Figure 1b implies the presence of randomly pinned moments during the ZFC process. Evidence for this hypothesis will be presented in the discussion section.

Figure 1b also displays a hyperbola-like inverse susceptibility ($\chi^{-1}(T)$) above T_C, a feature of FiM coupling.[26,27] Linear $\chi^{-1}(T)$ is found from 350 to 400 K. Curie-Weiss (CW) fitting, $1/\chi = (T − \theta)/C$, yields a Curie constant of $C = 1.86$ emu K^{-1} mol^{-1} Oe^{-1} and an effective moment of $\mu_{eff} = 3.85$ μ_B/f.u. A comparable value of μ_{eff} was found in analogous La_2NiIrO_6.[28] This value is apparently larger than the spin-only μ_{eff} of Ni^{2+} and Ir^{4+} (3.30 μ_B/f.u.). On the other hand, the branching ratio (BR = I_{L3}/I_{L2}) of Ir-XAS is 3.2 (Figure 1d). A BR value larger than the statistical value of 2 indicates a strong SOC and unquenched orbital moments.[29,30] Consequently, the orbital moment of Ir^{4+} contributes to the observed effective moment, explaining the deviation from the spin-only value.

Magnetic diffraction peaks observed by NPD at 4 K in Figure S2b (Supporting Information), also support long-range magnetic ordering. The magnetic diffraction peaks appear at the positions of crystallographic Bragg reflections, corresponding to magnetic satellites with propagation vector of $k = (0, 0, 0)$. The strong absorption of neutrons by Ir results in magnetic diffraction peaks too weak for a precise Rietveld refinement of the magnetic moments of Ir.[31] Nevertheless, the refinement results indicate that the magnetic moment localizes on Ni sites with 2.1(2) μ_B, and the magnetic moment lies in the a–c plane, forming an angle of 50±10° with the a-axis.

In order to better understand the magnetic properties of YNIO, we measured X-ray magnetic circular dichroism (XMCD), spectra at both Ir-$L_{2,3}$ and Ni-$L_{2,3}$ edges to determine the magnetic coupling between the Ir/Ni ions, and spin moment and orbital moment for each element separately.[24,25,32–36] Figure 1d and 1e display the XMCD spectra at the Ir-$L_{2,3}$ and Ni-$L_{2,3}$ edges, respectively. Using the sum rules we obtained: $M_{spin} = −0.046$, $M_{orb} = −0.033$ μ_B/Ir^{4+} and, $M_{spin} = 0.360$, $M_{orb} = 0.006$ μ_B/Ni^{2+} resulting in a total moment of 0.29

μ_B/f.u.,[37,38] that is consistent with bulk magnetization at 25 K (0.22 μ_B/f.u. in Figure S3c, Supporting Information). The opposite signs indicate that the moments of Ni and Ir are antiferromagnetically coupled. The Ni-spin obtained from the sum rule is notably smaller than 2.1 μ_B from NPD. Since XMCD measures the net magnetic moment, we attribute the reduced magnetic moments to the antiphase domains caused by the pinned moments as revealed by domain-structure analysis (vide infra). In other words, the ordered Ni and Ir magnetic moments (both spin and orbital), are underestimated by XMCD measurements under the present measuring conditions. Nevertheless, our XMCD results verify that the moments on Ni and Ir are antiferromagnetically coupled as displayed in Figure 1f. It is noteworthy that IrO_6 octahedra with a distortion of two short Ir–O bonds and four long Ir–O bonds allows for low spin Ir^{4+} $t_{2g}^5e_g^0$ with $(xy)^2(zx ± iyz)^3$ electronic configuration to retain an orbital angular momentum in many irridates.[19] As reported in the post-perovskite $CaIrO_3$ such octahedral distortion favors orbital-lattice coupling, and strong SOC with the orbital moment along the short Ir–O bonds.[19] There are also two short, 1.9844 Å and four long Ir–O bonds, 2.0020 and 2.0090 Å respectively, in YNIO. Hence the orbital moments are also expected to be along the short Ir–O bonds, forming an angle of ≈25° with the c-axis.

The M_{orb}/M_{spin} sum rule is another important criterion to testify SOC. The advantage of this criterion is that it does not require magnetic saturation and can be used even for paramagnetic and AFM materials.[39] The M_{orb}/M_{spin} sum rule follows Equation 1

$$\frac{M_{orb}}{M_{spin} + 7\langle T_z \rangle} = \frac{2\int_{L_3+L_2} (\sigma^+ − \sigma^-)d\omega}{3\int_{L_3} (\sigma^+ − \sigma^-)d\omega − 6\int_{L_2} (\sigma^+ − \sigma^-)d\omega} \quad (1)$$

where M_{orb} and M_{spin} are orbital and spin moments (μ_B/atom), respectively, σ^+ (σ^-) is the XAS intensity with the magnetic field parallel (antiparallel) to circular polarization of the incident light, and L_3 (L_2) indicates the integrated region of the XMCD spectrum. The term $7\langle T_z\rangle$ represents the intra-atomic dipole moment.[39] We obtain $M_{orb}/M_{spin} = 0.72$ for Ir^{4+} and 0.017 for Ni^{2+}. Note that we expect $M_{orb}/M_{spin} = 2$ for an octahedrally coordinated Ir^{4+} with $J_{eff} = 1/2$. The reduction of M_{orb}/M_{spin} from the expected value of 2 could be attributed to the nonnegligible multiplet interactions compared to the cubic crystal field effect.[24,40]

2.3. Exchange-Bias-Like Effect

Figure 2a shows hysteresis loops after different H_{FC} (0 Oe to 7 T) at 5 K. To be simplified, characteristic loops consisting of initial curves are plotted (see a full set of hysteresis loops in Figure S4a, Supporting Information). One can clearly see that centers of the loops move vertically along the M-axis. The VMS is quantified by $M_{shift} = 1/2(M^+ + M^-)$, where M^+ and M^- are positive and negative remnant magnetizations. The vertical shifts cause giant exchange-bias-like fields ($H_{EB} = 1/2(H_L + H_R)$) up to 1.7 T, due to the asymmetries of left (H_L) and right coercive fields (H_R). Symmetric downward vertical shifts are also found under negative cooling fields. Figure S5 (Supporting

ADVANCED
SCIENCE NEWS
www.advancedsciencenews.com
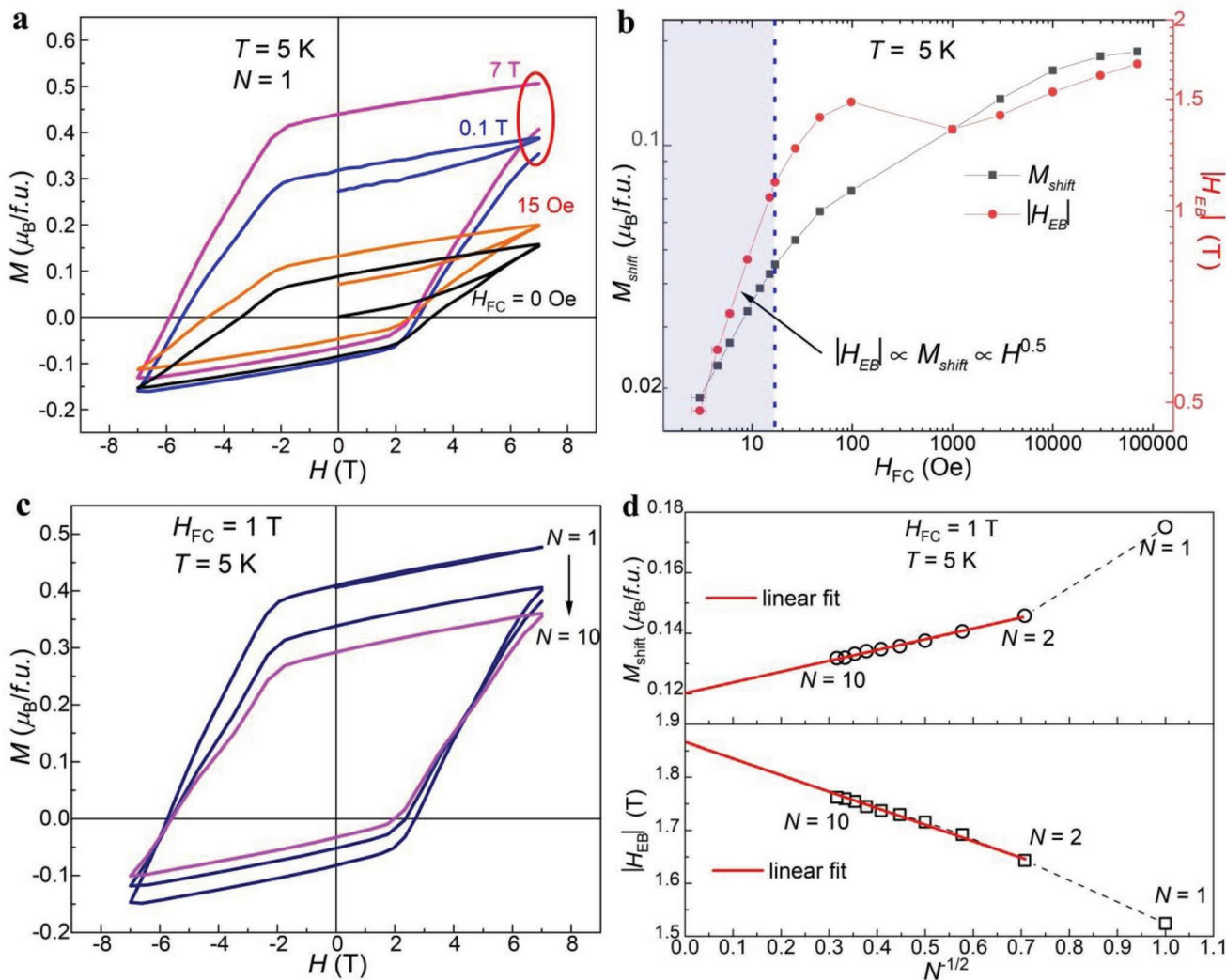
ADVANCED
MATERIALS
www.advmat.de

Figure 2. EB-like effects of YNIO at low temperature. a) Hysteresis loops at 5 K with H_{FC} varying from 0 Oe to 7 T. The red circle emphasizes the gaps on the loops. b) Summary of H_{FC} dependent M_{shift} and $|H_{EB}|$ at 5 K. c) Cycling number (N) dependence of hysteresis loops at 5 K under $H_{FC} = 1$ T. d) M_{shift} (top) and $|H_{EB}|$ (bottom) as functions of $N^{-1/2}$ under $H_{FC} = 1$ T. The red lines indicate linear fitting. The dashed lines are guides to the eye.

Information) shows hysteresis loops under cooling fields of 100 and −100 Oe at 5 K as a typical example. It is noteworthy that the bias-like phenomena of YNIO should be distinguished from conventional EB which are characterized by horizontal shifts of the centers of hysteresis loops.[7,19,41] The fascinating feature of YNIO is that M_{shift} and H_{EB} can be remarkably induced by tiny external fields of just a few Oersteds. The *log-log* plot of M_{shift} and $|H_{EB}|$ versus H_{FC} is shown in Figure 2b. The maximum increasing rate is found under extremely low H_{FC} (< 20 Oe), where both $|H_{EB}|$ and M_{shift} are proportional to $\sqrt{H_{FC}}$. A huge $|H_{EB}|$ of 1.1 T is obtained with $H_{FC} = 15$ Oe. The representative material $Mn_{3.5}Co_{0.5}N$ was reported to have an H_{EB} of 1.2 T with an H_{FC} of just 500 Oe. To obtain a comparable EB to that of YNIO, an H_{FC} is over 30 times larger than that of YNIO is required.[18] The high sensitivity of H_{EB} to extremely small H_{FC} implies potential technical applications of YNIO.

It is noteworthy that the hysteresis loops show visible gaps as marked by the red circle in Figure 2a once H_{FC} is larger than 0.1 T. After the first cycle, the magnetization at 7 T is not consistent

with that of the initial curve, which results in the gap. These gaps gradually vanish after several cycles (Figures S4b and S4c, Supporting Information). Similar gaps were found in both single phase and heterostructure systems.[18,42] Along with the closing gaps, the hysteresis loops steadily become flatter with increasing cycles (Figure 2c). This feature is reminiscent of the training effect in EB systems, demonstrating the decrease of EB following an empirical power law of N ($N > 1$).[18] A similar trend is applicable for M_{shift}. The power law fitting with Equation (2) is used:

$$M_{shift}(N) - M_{shift}^{\infty} \propto 1/\sqrt{N}(N > 1) \tag{2}$$

where M_{shift}^{∞} is M_{shift} in the limit of infinite loops. For instance, Figure 2d displays $N^{-1/2}$ dependence of M_{shift} under $T = 5$ K, $H_{FC} = 1$ T. The *y*-axis intercept of linear fit is $M_{shift}^{\infty} = 0.12$ μ_B/f.u.. In contrast, $|H_{EB}|$ increases with increasing N following Equation (3):

$$|H_{EB}^{\infty}| - |H_{EB}(N)| \propto 1/\sqrt{N}(N > 1) \tag{3}$$

**ADVANCED
SCIENCE NEWS**

www.advancedsciencenews.com

**ADVANCED
MATERIALS**

www.advmat.de

where $|H_{EB}^{\infty}|$ is $|H_{EB}|$ in the limit of infinite loops. Correspondingly, we obtain $|H_{EB}^{\infty}| = 1.86$ T in Figure 2d. The anomalous evolution of $|H_{EB}|$ again indicates that the EB-like behavior of YNIO is only the secondary effect due to the vertical shift of hysteresis loops and not a canonical EB effect.

The temperature dependence of M_{shift} and $|H_{EB}|$ was investigated under $H_{FC} = 0$, 0.01, and 7 T. For clarity, hysteresis loops under $H_{FC} = 100$ Oe at 5, 30 and 100 K are shown in **Figure 3**a as typical examples (see a full set of the loops along with the training effect in Figures S6 and S7, Supporting Information). The results are summarized in Figure 3b. Both the M_{shift} and $|H_{EB}|$ show non-monotonic changes with increasing temperature at a comparable rate. They undergo a drop below 30 K and then become robust again in a large temperature range, manifesting an advantage for potential applications. The onset temperature is ≈170 K, in the vicinity of T_C.

It is worth noting that a minor loop effect, i.e., unsaturated magnetic hysteresis loops, can naturally result in trivial shifts along H- and M-axes.[43] To rule out the minor loop effect, it is necessary to apply sufficient field to obtain saturated magnetization.[14] Given the large coercive fields at low temperature (5 K), it may require dozens of Tesla to achieve saturation. Alternately, saturation can be accomplished within ±7 T at high temperature range. Figure S8 (Supporting Information) displays the training hysteresis loops under $H_{FC} = 100$ Oe at 50 and 100 K respectively. It is clear that the loops saturate at ≈ ±5 T at both 50 and 100 K. After several cycles, the centers of the loops locate at the upper part of M-axes ($M_{shift} = 0.041$ and 0.035 μ_B/Mn respectively). In the case of saturation, there are only vertical rather than horizontal shifts in the hysteresis. These robust VMS at the high temperature range are incompatible with minor loops. Thus it is evidenced that although $M(H)$ at low temperature is in a minor loop due to unsaturation, the VMS does not originate only from the minor loop effect.

2.4. Domain Structures

To obtain a deeper insight of the intriguing magnetic properties, we used MFM to study the domain structures of YNIO after ZFC and FC processes. MFM images are measured at different magnetic fields that correspond to the points on the

$M(H)$ loops in **Figure 4**a. The corresponding topography images of the MFM measurements after ZFC and FC are present as Figure S9 (Supporting Information). The magnetic contrasts ($\Delta\varphi$) are represented by colors. The blue (red) area with negative (positive) $\Delta\varphi$ represents the net magnetization projecting along upward (downward) z direction, and the green area with nearly zero $\Delta\varphi$ represents domain walls or nonmagnetic grains with zero-magnetization.[44] For example, the large green area marked by the white circle in Figure 4b,c indicates a nonmagnetic Ir grain. To quantitatively demonstrate the magnetic state for each MFM image, we estimate the net magnetization by calculating the overall magnetic contrast ($\Delta\Phi$) with Equation (4):

$$\Delta\Phi = \frac{\Delta\Phi_{\uparrow} - \Delta\Phi_{\downarrow}}{\Delta\Phi_{\uparrow} + \Delta\Phi_{\downarrow}} \tag{4}$$

where $\Delta\Phi_{\uparrow}$ ($\Delta\Phi_{\downarrow}$) is the sum of positive (negative) $\Delta\Phi$ throughout an image. The evolution of $\Delta\Phi$ calculated from MFM images is proportional to the bulk magnetization measured by SQUID, as demonstrated in Figure 4a. At $H = 0$ T after ZFC, both upward and downward domains distribute randomly with size in micrometer in Figure 4b. The total area of upward domains is comparable to that of downward ones and we obtained $\Delta\Phi = -0.03(8)$, in agreement with an unmagnetized state in Figure 4a. When the field is increased to +2.5 T (Figure S10, Supporting Information), the distribution or size of either upward or downward domain barely changes with $\Delta\Phi = 0.03(6)$, indicating that most of the moments do not flip. Although the upward domains grow at $H = +7$ T (Figure 4c), $\Delta\Phi$ only increases to $\Delta\Phi = 0.32(5)$. The domain structures after ZFC and their evolution with applied magnetic field are consistent with small net magnetization.

In contrast, the MFM image under $H_{FC} = 0.1$ T is dominated by upward domains with smaller isolated downward ones (Figure 4d). The calculated $\Delta\Phi$ is 0.73(3), consistent with the large initial magnetization. In Figure 4e, an applied field of +7 T renders most of downward domains fragmentary and $\Delta\Phi$ increases to 0.88(2). When the field is reversed to −7 T, it is easier to find pinned moments. The majority of domains rotate their moments along the applied field direction as shown in Figure 4f. However, by carefully comparing Figure 4e,f, one can note that some domains keep their moments along the upward z direction (some representative ones are marked by the dashed
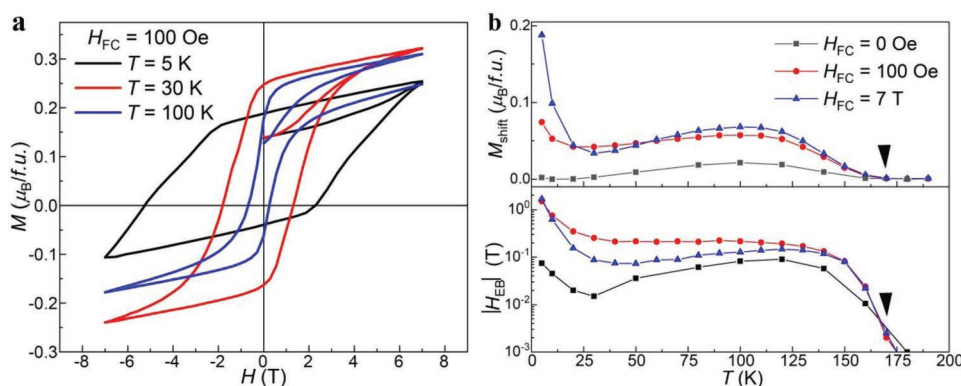

Figure 3. Temperature dependence of EB-like effects. a) Hysteresis loops under $H_{FC} = 100$ Oe at 5, 30, and 100 K. b) Temperature dependence of M_{shift} (top) and $|H_{EB}|$ (bottom) under $H_{FC} = 0$, 0.01, and 7 T. The black triangles at 170 K indicate the highest temperature to observe the exchange-bias effect.
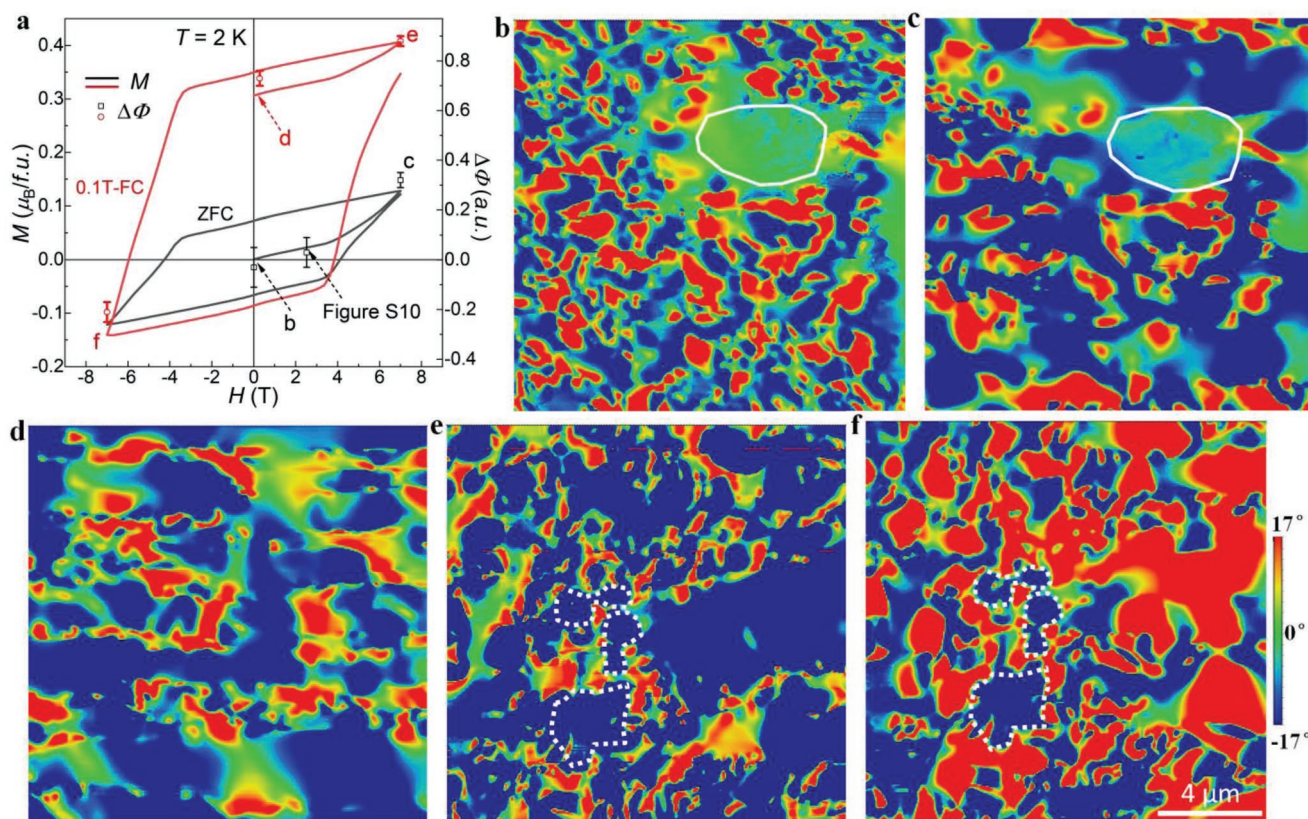
Figure 4. Hysteresis loops and corresponding domain structures. a) $M(H)$ at 2 K after ZFC and 0.1 T FC. The letters represent corresponding figures. b–f) MFM images with size of $15 \times 15 \ \mu m^2$ at 1.6 K showing magnetic domain structures at 0 T (b) and 7 T (c) after zero field cooling, 0.1 T (d), 7 T (e), and −7 T (f) after 0.1 T field cooling. The color bar is $\pm 17°$ for phase shift, and the scale bar is 4 µm.

circles in Figure 4e,f). Consequently, the net moments are offset with $\Delta\Phi = -0.21(4)$, leading to a remarkable VMS.

2.5. Physical Mechanism

We observed evidence of pinned moments via MFM imaging. As discussed above, in YNIO the IrO_6 octahedral distortion allows for orbital-lattice coupling and the orbital moment along the short Ir–O bonds. The strong SOC is revealed by the large BR and M_{orb}/M_{spin}. We propose that the spins of Ir are locked with the orbital moments due to the strong SOC. The spins of Ni are anchored with those of Ir by AFM exchange interactions between the two sublattices. Consequently, all the magnetic moments in YNIO are pinned. The pinned moments result in a huge anisotropy energy which prevents the rotation of moments or the movements of the domain walls. This scenario is consistent with a well-established picture that orbital moments and strong SOC are essential for large magnetic anisotropy.[45]

Thus the initial magnetic state has a major influence on the magnetization of YNIO. After ZFC process, domains with upward moments are balanced by those with downward ones as evidenced by the MFM image; at 2 K such frozen domains are retained below 3.5 T (Figure 4a). This observation also explains the nearly zero magnetization of the ZFC curve at 0.1 T and the large irreversibility between ZFC and FC in

Figure 1b. With field increasing beyond the upturn point as marked in Figure 4a, domains begin to merge together, and the larger domain size increases the anisotropy energy. Then a larger inverse field is required to flip the domains and the spontaneous VMS appears.

Under FC process, the domains have been rotated along the direction of the applied cooling fields. During the loop process, the inverse field of −7 T is not strong enough to completely overcome the huge anisotropy energy and the domains with upward moments are only partially reduced (Figure 4f). Subsequently, rotation of magnetization is incomplete and a vertical shift emerges. Furthermore, the domains become extended with larger H_{FC}. As the anisotropy energy is also proportional to domain size, a larger external field is required to rotate the domains. As a result, the VMS is enhanced by increasing H_{FC}.

3. Conclusion

The new B-site ordered double perovskite, Y_2NiIrO_6 (YNIO) shows long-range FiM ordering below $T_C \approx 192$ K, with antiparallel moments between Ni^{2+} and Ir^{4+}. It is noteworthy, that a small $H_{FC} = 15$ Oe induces a significant vertical shift of the magnetic loop, which in turn results in the huge asymmetry of left and right coercive fields to induce an EB-like field of 1.1 T. The VMS appears in the vicinity of T_C and becomes robust below 170 K. Strong SOC and ordering of orbital moment on

Ir^{4+} are confirmed by XMCD, and the latter is coupled with distorted IrO_6 octahedra. The spins on Ir and Ni are locked due to the SOC and AFM magnetic exchange interactions, respectively. It is proposed that pinned moments in YNIO, which are evidenced by MFM images, are the key mechanism to induce VMS. Different from conventional bilayer systems, where EB is produced by the pinned spins at the interface, in YNIO the pinned moments are present throughout the full volume. It is notable that the domain sizes are limited to the order of micrometers due to the finite grain sizes in polycrystalline YNIO samples. It is expected that the pinning of magnetic domains would be more remarkable in single crystal bulks or thin films, in which larger domains and correspondingly higher anisotropy energies are antipated. The unusual VMS and the pinning of magnetic domains represent YNIO as an intriguing material to study magnetic coupling in the presence of orbital magnetization and spin–orbit coupling.

4. Experimental Section

Sample Synthesis and Basic Characterizations: Polycrystalline YNIO samples were synthesized under high-temperature and high-pressure conditions (1473–1573 K and 6–8.5 GPa). The well ground mixture of Y_2O_3 (Alfa Aesar, 99.9%), NiO (Alfa Aesar, 99.9%), and IrO_2 (Alfa Aesar, 99.9%) was pelletized and then loaded in Pt capsules. After reactions, the pressures were maintained during the temperature quenching and then decompressed slowly. Phase purity and crystal structure were determined with laboratory PXD. Rietveld refinements were performed with GSAS software packages.[46] dc magnetization was measured with a Quantum Design Superconducting Quantum Interference Device (SQUID, MPMS3). Temperature-dependent magnetization ($M(T)$) and magnetic hysteresis loops ($M(H)$) were measured under both ZFC and FC processes. The residual field that is trapped in the superconducting magnet was carefully balanced to be ± 0.5 Oe with the following: (1) setting magnetic field to the upper limit, +7 T; (2) reducing the field to 0.5 T; (3) removing the field in the oscillating mode; (4) setting the field to 3 Oe. ac susceptibility and heat capacity measurements were conducted with a Quantum Design Physical Property Measurement System (PPMS). Sample crystallinity and morphology were studied with scanning electron microscopy (SEM Zeiss 550) and transmission electron microscopy (TEM JEOL 2100F).

Time-of-Flight Neutron Powder Diffraction: NPD was performed at the time-of-flight general purpose powder diffractometer at China Spallation Neutron Source, and neutron diffraction patterns were collected with wavelength band from 0.1 to 4.9 Å. The crystal and magnetic structures were refined by the Rietveld method using GSAS software packages.[46]

X-ray Absorption Spectroscopy and X-ray Magnetic Circular Dichroism: The Ir-L_3 XAS was measured at 300 K at beamline P09 at PETRA III at DESY in Hamburg. The Ir-$L_{2,3}$ XMCD was measured at 10 K and 5 T. The Ni-$L_{2,3}$ XMCD was measured at 25 K and 6 T at beamline BL29 BOREAS of the ALBA synchrotron near Barcelona.[47]

Magnetic Force Microscopy: MFM measurements were carried out in a variable temperature system from Attocube (attoDRY2100) equipped with a superconducting magnet. The magnetic field was applied out-of-plane to the sample with maximal value of up to 7 T. A positive magnetic field was along the upward z direction. All measurements were carried out in low pressure helium environment with a large quality factor of the cantilever that allows for high force sensitivity. A magnetic probe from Nanosensors (PPP-MFMR) was used for imaging the magnetic textures using a phase modulation technique in noncontact mode. MFM imaging was carried out in two steps. First, the tilt and misalignment of the sample was corrected and topography was acquired. Then, to measure magnetic forces, the cantilever was retracted from the sample surface and scanned at a fixed lift height of 50 nm.

Supporting Information

Supporting Information is available from the Wiley Online Library or from the author.

Conflict of Interest

The authors declare no conflict of interest.

Data Availability Statement

The data that support the findings of this study are available from the corresponding author upon reasonable request.

[1] S. M. Wu, S. A. Cybart, P. Yu, M. D. Rossell, J. X. Zhang, R. Ramesh, R. C. Dynes, *Nat. Mater.* **2010**, *9*, 756.

[2] X. He, Y. Wang, N. Wu, A. N. Caruso, E. Vescovo, K. D. Belashchenko, P. A. Dowben, C. Binek, *Nat. Mater.* **2010**, *9*, 579.

[3] L. Wei, Z. Hu, G. Du, Y. Yuan, J. Wang, H. Tu, B. You, S. Zhou, J. Qu, H. Liu, R. Zheng, Y. Hu, J. Du, *Adv. Mater.* **2018**, *30*, 1801885.

[4] J. Kang, J. Ryu, J.-G. Choi, T. Lee, J. Park, S. Lee, H. Jang, Y. S. Jung, K.-J. Kim, B.-G. Park, *Nat. Commun.* **2021**, *12*, 6420.

[5] S. Peng, D. Zhu, W. Li, H. Wu, A. J. Grutter, D. A. Gilbert, J. Lu, D. Xiong, W. Cai, P. Shafer, K. L. Wang, W. Zhao, *Nat. Electron.* **2020**, *3*, 757.

[6] Y. Wu, W. Wang, L. Pan, K. L. Wang, *Adv. Mater.* **2022**, *34*, 2105266.

[7] J. Nogués, I. K. Schuller, *J. Magn. Magn. Mater.* **1999**, *192*, 203.

[8] M. Gibert, P. Zubko, R. Scherwitzl, J. Iniguez, J.-M. Triscone, *Nat. Mater.* **2012**, *11*, 195.

[9] H. Ohldag, A. Scholl, F. Nolting, E. Arenholz, S. Maat, A. T. Young, M. Carey, J. Stohr, *Phys. Rev. Lett.* **2003**, *91*, 017203.

[10] Y. Shiratsuchi, H. Noutomi, H. Oikawa, T. Nakamura, M. Suzuki, T. Fujita, K. Arakawa, Y. Takechi, H. Mori, T. Kinoshita, M. Yamamoto, R. Nakatani, *Phys. Rev. Lett.* **2012**, *109*, 077202.

[11] J. Hjorth, J. Sollerman, P. Moller, J. P. Fynbo, S. E. Woosley, C. Kouveliotou, N. R. Tanvir, J. Greiner, M. I. Andersen, A. J. Castro-Tirado, J. M. Castro Ceron, A. S. Fruchter, J. Gorosabel, P. Jakobsson, L. Kaper, S. Klose, N. Masetti, H. Pedersen, K. Pedersen, E. Pian, E. Palazzi, J. E. Rhoads, E. Rol, E. P. van den Heuvel, P. M. Vreeswijk, D. Watson, R. A. M. J. Wijers, *Nature* **2003**, *423*, 847.

[12] M. Ali, P. Adie, C. H. Marrows, D. Greig, B. J. Hickey, R. L. Stamps, *Nat. Mater.* **2007**, *6*, 70.

[13] H. K. Gweon, S. Y. Lee, H. Y. Kwon, J. Jeong, H. J. Chang, K.-W. Kim, Z. Q. Qiu, H. Ryu, C. Jang, J. W. Choi, *Nano Lett.* **2021**, *21*, 1672.

[14] X. F. Zhou, X. Z. Chen, Y. F. You, L. Y. Liao, H. Bai, R. Q. Zhang, Y. J. Zhou, H. Q. Wu, C. Song, F. Pan, *Phys. Rev. Appl.* **2020**, *14*, 054037.

[15] E. Maniv, R. A. Murphy, S. C. Haley, S. Doyle, C. John, A. Maniv, S. K. Ramakrishna, Y.-L. Tang, P. Ercius, R. Ramesh, A. P. Reyes, J. R. Long, J. G. Analytis, *Nat. Phys.* **2021**, *17*, 525.

[16] A. K. Nayak, M. Nicklas, S. Chadov, P. Khuntia, C. Shekhar, A. Kalache, M. Baenitz, Y. Skourski, V. K. Guduru, A. Puri, U. Zeitler, J. M. D. Coey, C. Felser, *Nat. Mater.* **2015**, *14*, 679.

[17] A. K. Nayak, M. Nicklas, S. Chadov, C. Shekhar, Y. Skourski, J. Winterlik, C. Felser, *Phys. Rev. Lett.* **2013**, *110*, 127204.

[18] L. Ding, L. Chu, P. Manuel, F. Orlandi, M. Li, Y. Guo, Z. Liu, *Mater. Horiz.* **2019**, *6*, 318.

[19] J.-G. Cheng, J.-S. Zhou, J. B. Goodenough, Y. Sui, Y. Ren, M. R. Suchomel, *Phys. Rev. B* **2011**, *83*, 064401.

[20] G. van der Laan, B. T. Thole, G. A. Sawatzky, M. Verdaguer, *Phys. Rev. B* **1988**, *37*, 6587(R).

[21] M. W. Haverkort, S. I. Csiszar, Z. Hu, S. Altieri, A. Tanaka, H. H. Hsieh, H.-J. Lin, C. T. Chen, T. Hibma, L. H. Tjeng, *Phys. Rev. B* **2004**, *69*, 020408(R).

[22] H. Guo, Z. W. Li, L. Zhao, Z. Hu, C. F. Chang, C.-Y. Kuo, W. Schmidt, A. Piovano, T. W. Pi, O. Sobolev, D. I. Khomskii, L. H. Tjeng, A. C. Komarek, *Nat. Commun.* **2018**, *9*, 43.

[23] K. Baroudi, C. Yim, H. Wu, Q. Huang, J. H. Roudebush, E. Vavilova, H.-J. Grafe, V. Kataev, B. Buechner, H. Ji, C. Kuo, Z. Hu, T.-W. Pi, C. Pao, J. Lee, D. Mikhailova, L. Hao Tjeng, R. J. Cava, *J. Solid State Chem.* **2014**, *210*, 195.

[24] S. Agrestini, C. Y. Kuo, K. Chen, Y. Utsumi, D. Mikhailova, A. Rogalev, F. Wilhelm, T. Förster, A. Matsumoto, T. Takayama, H. Takagi, M. W. Haverkort, Z. Hu, L. H. Tjeng, *Phys. Rev. B* **2018**, *97*, 214436.

[25] S. Agrestini, K. Chen, C.-Y. Kuo, L. Zhao, H.-J. Lin, C.-T. Chen, A. Rogalev, P. Ohresser, T.-S. Chan, S.-C. Weng, G. Auffermann, A. Völzke, A. C. Komarek, K. Yamaura, M. W. Haverkort, Z. Hu, L. H. Tjeng, *Phys. Rev. B* **2019**, *100*, 014443.

[26] Z. Deng, M. Retuerto, S. Liu, M. Croft, P. W. Stephens, S. Calder, W. Li, B. Chen, C. Jin, Z. Hu, M.-R. Li, H.-J. Lin, T.-S. Chan, C.-T. Chen, S. W. Kim, M. Greenblatt, *Chem. Mater.* **2018**, *30*, 7047.

[27] Z. Deng, C. J. Kang, M. Croft, W. Li, X. Shen, J. Zhao, R. Yu, C. Jin, G. Kotliar, S. Liu, T. A. Tyson, R. Tappero, M. Greenblatt, *Angew. Chem., Int. Ed.* **2020**, *59*, 8240.

[28] J. Song, B. Zhao, L. Yin, Y. Qin, J. Zhou, D. Wang, W. Song, Y. Sun, *Dalton Trans.* **2017**, *46*, 11691.

[29] Q. Cui, J.-G. Cheng, W. Fan, A. E. Taylor, S. Calder, M. A. McGuire, J.-Q. Yan, D. Meyers, X. Li, Y. Q. Cai, Y. Y. Jiao, Y. Choi, D. Haskel, H. Gotou, Y. Uwatoko, J. Chakhalian, A. D. Christianson, S. Yunoki, J. B. Goodenough, J.-S. Zhou, *Phys. Rev. Lett.* **2016**, *117*, 176603.

[30] M. A. Laguna-Marco, D. Haskel, N. Souza-Neto, J. C. Lang, V. V. Krishnamurthy, S. Chikara, G. Cao, M. van Veenendaal, *Phys. Rev. Lett.* **2010**, *105*, 216407.

[31] P. Kayser, A. Muñoz, J. L. Martínez, F. Fauth, M. T. Fernández-Díaz, J. A. Alonso, *Acta Mater.* **2021**, *207*, 116684.

[32] X. Wang, M. Liu, X. Shen, Z. Liu, Z. Hu, K. Chen, P. Ohresser, L. Nataf, F. Baudelet, H. J. Lin, C. T. Chen, Y. L. Soo, Y. F. Yang, C. Jin, Y. Long, *Inorg. Chem.* **2019**, *58*, 320.

[33] H. L. Feng, M. P. Ghimire, Z. Hu, S.-C. Liao, S. Agrestini, J. Chen, Y. Yuan, Y. Matsushita, Y. Tsujimoto, Y. Katsuya, M. Tanaka, H.-J. Lin, C.-T. Chen, S.-C. Weng, M. Valvidares, K. Chen, F. Baudelet, A. Tanaka, M. Greenblatt, L. H. Tjeng, K. Yamaura, *Phys. Rev. Mater.* **2019**, *3*, 124404.

[34] H. L. Feng, J. Chen, Z. Hu, X. Wang, M. Reehuis, P. Adler, A. Hoser, M.-X. Wu, S. Agrestini, H. B. Vasili, J. Herrero-Martin, L. Nataf, F. Baudelet, K. Chen, Y. Matsushita, M.-R. Li, L. H. Tjeng, C. Felser, M. Jansen, K. Yamaura, *Phys. Rev. Mater.* **2020**, *4*, 064420.

[35] J. Chen, X. Wang, Z. Hu, L. H. Tjeng, S. Agrestini, M. Valvidares, K. Chen, L. Nataf, F. Baudelet, M. Nagao, Y. Inaguma, A. A. Belik, Y. Tsujimoto, Y. Matsushita, T. Kolodiazhnyi, R. Sereika, M. Tanaka, K. Yamaura, *Phys. Rev. B* **2020**, *102*, 184418.

[36] Z. Liu, X. Wang, X. Ye, X. Shen, Y. Bian, W. Ding, S. Agrestini, S.-C. Liao, H.-J. Lin, C.-T. Chen, S.-C. Weng, K. Chen, P. Ohresser, L. Nataf, F. Baudelet, Z. Sheng, S. Francoual, J. R. L. Mardegan, O. Leupold, Z. Li, X. Xi, W. Wang, L. H. Tjeng, Z. Hu, Y. Long, *Phys. Rev. B* **2021**, *103*, 014414.

[37] B. T. Thole, P. Carra, F. Sette, G. van der Laan, *Phys. Rev. Lett.* **1992**, *68*, 1943.

[38] P. Carra, B. T. Thole, M. Altarelli, X. Wang, *Phys. Rev. Lett.* **1993**, *70*, 694.

[39] J. Stohr, H. Konig, *Phys. Rev. Lett.* **1995**, *75*, 3748.

[40] S. Agrestini, C.-Y. Kuo, K.-T. Ko, Z. Hu, D. Kasinathan, H. B. Vasili, J. Herrero-Martin, S. M. Valvidares, E. Pellegrin, L.-Y. Jang, A. Henschel, M. Schmidt, A. Tanaka, L. H. Tjeng, *Phys. Rev. B* **2017**, *96*, 161107(R).

[41] D. Deng, J. Zheng, D. Yu, B. Wang, D. Sun, M. Avdeev, Z. Feng, C. Jing, B. Lu, W. Ren, S. Cao, J. Zhang, *Appl. Phys. Lett.* **2015**, *107*, 102404.

[42] M. Buchner, B. Henne, V. Ney, A. Ney, *Phys. Rev. B* **2019**, *99*, 064409.

[43] L. Pi, S. Zhang, S. Tan, Y. Zhang, *Appl. Phys. Lett.* **2006**, *88*, 1025.

[44] Y. Ba, S. Zhuang, Y. Zhang, Y. Wang, Y. Gao, H. Zhou, M. Chen, W. Sun, Q. Liu, G. Chai, J. Ma, Y. Zhang, H. Tian, H. Du, W. Jiang, C. Nan, J.-M. Hu, Y. Zhao, *Nat. Commun.* **2021**, *12*, 322.

[45] R. Skomski, A. Kashyap, A. Enders, *J. Appl. Phys.* **2011**, *109*, 07E143.

[46] B. H. Toby, *J. Appl. Crystallogr.* **2001**, *34*, 210.

[47] A. Barla, J. Nicolas, D. Cocco, S. M. Valvidares, J. Herrero-Martin, P. Gargiani, J. Moldes, C. Ruget, E. Pellegrin, S. Ferrer, *J. Synchrotron Rad.* **2016**, *23*, 1507.